http://www.iop.org/journals/ppcf
http://stacks.iop.org/ppcf/46/1197

# Predictive transport modelling of type I ELMy H-mode dynamics using a theory-motivated combined ballooning–peeling model

**J-S Lönnroth**[1]**, V Parail**[2]**, A Dnestrovskij**[3]**, C Figarella**[4]**, X Garbet**[4]**, H Wilson**[2] **and JET-EFDA Contributors**

[1] Association EURATOM-Tekes, Helsinki University of Technology, PO Box 2200, 02015 HUT, Finland
[2] EURATOM/UKAEA Fusion Association, Culham Science Centre, Abingdon, Oxfordshire OX14 3DB, UK
[3] Russian Science Centre, Kurchatov Institute, Moscow, Russia
[4] Association EURATOM-CEA, CEA Cadarache, DRFC, 13108 Saint-Paul-Lez-Durance, France

## Abstract

This paper discusses predictive transport simulations of the type I ELMy high confinement mode (H-mode) with a theory-motivated edge localized mode (ELM) model based on linear ballooning and peeling mode stability theory. In the model, a total mode amplitude is calculated as a sum of the individual mode amplitudes given by two separate linear differential equations for the ballooning and peeling mode amplitudes. The ballooning and peeling mode growth rates are represented by mutually analogous terms, which differ from zero upon the violation of a critical pressure gradient and an analytical peeling mode stability criterion, respectively. The damping of the modes due to non-ideal magnetohydrodynamic effects is controlled by a term driving the mode amplitude towards the level of background fluctuations. Coupled to simulations with the JETTO transport code, the model qualitatively reproduces the experimental dynamics of type I ELMy H-mode, including an ELM frequency that increases with the external heating power. The dynamics of individual ELM cycles is studied. Each ELM is usually triggered by a ballooning mode instability. The ballooning phase of the ELM reduces the pressure gradient enough to make the plasma peeling unstable, whereby the ELM continues driven by the peeling mode instability, until the edge current density has been depleted to a stable level. Simulations with current ramp-up and ramp-down are studied as examples of situations in which pure peeling and pure ballooning mode ELMs, respectively, can be obtained. The sensitivity with respect to the ballooning and peeling mode growth rates is investigated. Some consideration is

also given to an alternative formulation of the model as well as to a pure peeling model.

(Some figures in this article are in colour only in the electronic version)

## 1. Introduction

The high confinement mode (H-mode) offers a promising regime of operation for tokamak plasmas. H-mode operation is characterized by the formation of an edge transport barrier (ETB), a thin layer with suppressed anomalous transport just inside the magnetic separatrix, resulting in a steep edge pressure gradient and improved confinement. The ETB generally features strong periodic bursts of particles and energy, referred to as edge localized modes (ELMs) [1, 2], which limit the achievable level of pressure gradient. ELMs have the beneficial effect of transporting impurities across the pedestal region, thus helping to prevent the plasma from terminating due to impurity accumulation. However, ELM crashes, especially type I ELM crashes, also have the disadvantage of causing large peak heat loads on the divertor plates, which can be a serious problem in large tokamaks. ELMs are broadly believed to be controlled by a combination of magnetohydrodynamic (MHD) ballooning mode instabilities driven mainly by the edge pressure gradient and peeling mode instabilities driven mainly by the edge current. The most commonly occurring type of ELMs, called type I ELMs, have been observed for a wide range of densities in plasmas with modest and strong external heating. Type I ELMs are the most violent type of ELM events. They are capable of removing up to 10% of the plasma energy in a single ELM and are characterized by an ELM frequency that increases with the power flux across the last closed flux surface.

Many different approaches have been used in predictive transport modelling of type I ELMy H-mode. Qualitatively, the main features of type I ELMy H-mode can be reproduced fairly well even with a very simple ad hoc model, in which the transport coefficients are enhanced uniformly throughout the ETB to an arbitrary level for an arbitrary duration of time once a pressure gradient threshold has been exceeded [3–5]. In such simulations, the ELM amplitude and ELM duration have simply been chosen so that each individual ELM removes an appropriate amount of plasma energy and the critical pressure gradient has typically been set to match the finite $n$ ballooning stability limit determined by MHD stability analysis. It is usually assumed that the ELMs are controlled by the pressure gradient, but the influence of current-driven modes can to some extent be accounted for implicitly by determining the finite $n$ ballooning stability limit in a complete analysis taking into account the current as well. This crude ad hoc approach can to some extent be refined, e.g. by using Gaussian-shaped ELMs consistent with linear theory and by adjusting the ELM width in accordance with mode widths derived from linear MHD [6]. Apart from in simulations with a stability limit only for ballooning modes, the simple ad hoc ELM modelling scheme has also recently been used in simulations with stability criteria for both ballooning and peeling modes [7]. In more sophisticated ELM modelling approaches, the times of ELM onset as well as the ELM amplitude and ELM duration have been self-consistently calculated from a simple model of instability. Such modelling has recently been carried out by coupling a transport simulation to a model for the amplitude of an unstable ballooning mode in a system with a background noise [8].

This paper takes the idea of coupling a simple model of instability to a transport simulation one step further than previous studies by introducing a theory-motivated instability model with both ballooning and peeling mode components in the simulations. The modelling scheme can

qualitatively reproduce the experimental dynamics of type I ELMy H-mode. In particular, the dynamics of individual ELM cycles is studied in this paper. The behaviour of the model in simulations with current ramp-up and ramp-down and in various parameter scans is also investigated.

## 2. Theory-motivated ELM models based on ballooning and/or peeling mode stability

In the predictive transport modelling presented in this paper, a simple theory-motivated model based on linear ballooning and peeling mode stability theory is used to describe the dynamics of type I ELM generation. The use of an alternative formulation of the model as well as of a pure peeling model is also briefly demonstrated. The construction of these models is inspired by and analogous to the construction of similar models used in previous studies. Specifically, the construction of the model

$$\frac{d\xi}{dt} = \lambda(|p'| - |p'_c| + av_\theta^2 - bv'^2_E)\xi \tag{1}$$

for the amplitude of an unstable ballooning mode used in [9] serves as a starting point, as in [8]. Here, $\xi$ is the mean squared level of normalized MHD velocity fluctuations, $t$ is the time and the expression in front of $\xi$ on the right-hand side corresponds to the growth rate of the ballooning instability. The quantity $\lambda$ is a parameter characterizing the growth rate, $p'$ is the pressure gradient and $p'_c$ is a critical pressure gradient, above which the instability develops. The last two terms inside the parentheses represent corrections due to poloidal rotation and the shear in the flow of $\boldsymbol{E} \times \boldsymbol{B}$ motion, respectively, both of which modify the stability threshold. In this paper, the equations used to describe the time evolution of the ballooning and peeling mode amplitudes have the format of the pure ballooning model

$$\frac{d\xi}{dt} = C_b \frac{c_s}{\sqrt{L_p R}} \left(1 - \frac{\alpha_c}{\alpha}\right) H \left(1 - \frac{\alpha_c}{\alpha}\right) \xi - C_d \frac{c_s}{R}(\xi - \xi_0) \tag{2}$$

previously introduced in [8] and constructed analogously to equation (1). Here, $C_b \sim 1$, $C_d \sim 0.1$ and $\xi_0 \sim 0.01$ are constants characterizing the growth rate of the ballooning mode instability, the decay rate of the mode due to non-ideal MHD effects and the level of background fluctuations, respectively, $H$ is the Heaviside function defined as $H(x) = 0$, if $x < 0$ and $H(x) = 1$, if $x \geqslant 0$, $x$ being an arbitrary variable, $c_s = \sqrt{T_{ele}/m_{ion}}$ is the sound speed, where $T_{ele}$ is the electron temperature and $m_{ion}$ is the ion mass, $L_p = p/p'$ is the pressure scale length, where $p$ is the pressure, $R$ is the major radius, $\alpha = -(2\mu_0 r^2/B_\theta)(dp/d\psi)/0.64$ is the normalized pressure gradient, where $r$ is the minor radius, $B_\theta$ is the poloidal magnetic field and $\psi$ is the poloidal flux coordinate, and $\alpha_c$ is the critical normalized pressure gradient.

In the pure ballooning model given by equation (2), the stability threshold has been described by a fixed critical pressure gradient, which can be a reasonable approximation in certain circumstances. Similarly, one could use a fixed critical current as the stability threshold in a pure peeling model as a first approximation. However, [10] proposes a more general localized peeling stability criterion based on the MHD energy principle. By denoting

$$J = 1 + \frac{1}{\pi q'} \oint \frac{j_\parallel B}{R^2 B_\theta^3} dl - \Delta_v, \tag{3}$$

$$J_c = \sqrt{1 - 4D_M}, \tag{4}$$

the condition for peeling stability can be expressed as

$$J < J_c. \tag{5}$$

Here, $D_{\mathrm{M}}$ is the Mercier index [11, 12], which is proportional to the pressure gradient $p'$, $q'$ is the gradient of the safety factor, $j_{\parallel}$ is the current density parallel to the magnetic field, $B$ is the magnetic field strength and $\Delta_{\mathrm{v}}$ is a vacuum energy parameter describing the distance from the external surface to the plasma surface.

Assuming equation (5) to be the criterion for peeling stability, the following linear differential equation for the peeling mode amplitude, completely analogous to equation (2) for the ballooning mode amplitude, has been constructed to describe the dynamics of peeling-driven ELMs:

$$\frac{\mathrm{d}\xi}{\mathrm{d}t} = C_{\mathrm{p}}\gamma_{\mathrm{p}}\left(1 - \frac{J_{\mathrm{c}}}{J}\right)H(J - J_{\mathrm{c}})\xi - C_{\mathrm{d}}\frac{c_{\mathrm{s}}}{R}(\xi - \xi_0). \tag{6}$$

Here, $C_{\mathrm{p}} \sim 1$ is a constant characterizing the growth rate of the peeling mode instability and $\gamma_{\mathrm{p}}$ is the characteristic peeling mode growth rate.

In the construction of equation (6) (as well as in the construction of equation (2)), the corrections to critical pressure gradient due to plasma rotation used in equation (1) have been omitted for simplicity. Above the threshold $J_{\mathrm{c}}$, the mode amplitude $\xi$ increases exponentially. Below the threshold, the growth rate is zero due to the Heaviside function, which, as in equation (2), has been introduced in the model to account for the fact that there is no damping or growing solution in ideal MHD below the instability threshold. Introducing the Heaviside function is a simple way to reproduce the transition from an oscillating solution to a growing solution taking place when the instability threshold is exceeded. The second term on the right-hand side of equation (6) describes the level of background fluctuations and the decay rate of the mode after an ELM relaxation due to non-ideal MHD effects. It causes the mode amplitude to tend to converge towards the level of background fluctuations between the ELMs. The coefficient $C_{\mathrm{d}}c_{\mathrm{s}}/R$ determines the rate at which the mode is damped after an ELM crash by, e.g. finite viscosity, diffusivity and other non-ideal MHD effects.

In the most complete scenario, in which it is assumed that the ELMs can be driven by ballooning modes, peeling modes or combinations of both types of instabilities, equations (2) and (6) are solved separately for the ballooning and peeling mode amplitudes $\xi_{\mathrm{b}}$ and $\xi_{\mathrm{p}}$, respectively, whereupon the individual mode amplitudes are added to give a total mode amplitude $\xi$:

$$\frac{\mathrm{d}\xi_{\mathrm{b}}}{\mathrm{d}t} = C_{\mathrm{b}}\gamma_{\mathrm{b}}\left(1 - \frac{\alpha_{\mathrm{c}}}{\alpha}\right)H(\alpha - \alpha_{\mathrm{c}})\xi_{\mathrm{b}} - C_{\mathrm{d}}\frac{c_{\mathrm{s}}}{R}(\xi_{\mathrm{b}} - \xi_0), \tag{7}$$

$$\frac{\mathrm{d}\xi_{\mathrm{p}}}{\mathrm{d}t} = C_{\mathrm{p}}\gamma_{\mathrm{p}}\left(1 - \frac{J_{\mathrm{c}}}{J}\right)H(J - J_{\mathrm{c}})\xi_{\mathrm{p}} - C_{\mathrm{d}}\frac{c_{\mathrm{s}}}{R}(\xi_{\mathrm{p}} - \xi_0), \tag{8}$$

$$\xi = \xi_{\mathrm{b}} + \xi_{\mathrm{p}}. \tag{9}$$

Here, $\gamma_{\mathrm{b}}$ is the ballooning mode growth rate. In this paper, $\gamma_{\mathrm{b}} = c_{\mathrm{s}}/\sqrt{L_{\mathrm{p}}R}$ has generally been used for the ballooning mode growth rate and, for simplicity, $\gamma_{\mathrm{p}} = \gamma_{\mathrm{b}}$ for the peeling mode growth rate. Again, $C_{\mathrm{b}} \sim 1$, $C_{\mathrm{p}} \sim 1$, $C_{\mathrm{d}} \sim 0.1$. The simplification $\gamma_{\mathrm{p}} = \gamma_{\mathrm{b}}$ can be used, because the models defined by equations (6) and (7)–(9) are relatively insensitive to the growth rates, as will be shown in section 4.4.

Assuming that there is non-linear coupling between the ballooning and peeling modes, equations (7)–(9) can be replaced with a single differential equation for a combined ballooning and peeling mode amplitude:

$$\frac{\mathrm{d}\xi}{\mathrm{d}t} = C_{\mathrm{b}}\gamma_{\mathrm{b}}\left(1 - \frac{\alpha_{\mathrm{c}}}{\alpha}\right)H(\alpha - \alpha_{\mathrm{c}})\xi + C_{\mathrm{p}}\gamma_{\mathrm{p}}\left(1 - \frac{J_{\mathrm{c}}}{J}\right)H(J - J_{\mathrm{c}})\xi - C_{\mathrm{d}}\frac{c_{\mathrm{s}}}{R}(\xi - \xi_0). \tag{10}$$

In this model, the mode amplitude starts to grow exponentially as soon as either instability threshold is exceeded. The damping mechanism is the same as in the individual

equations (7) and (8). As will be discussed in section 4.4, the one-equation ballooning–peeling model given by equation (10) almost always reproduces the same ELM dynamics as the model with separate equations for ballooning and peeling modes given by equations (7)–(9).

## 3. JETTO implementation

The predictive transport simulations presented in this paper have been carried out using the 1.5D JETTO transport code [13] coupled with the theory-motivated ELM models based on linear ballooning and peeling mode stability theory defined in the preceding section. The transport model used in the JETTO simulations is the so-called JET transport model, a mixed Bohm/gyro-Bohm model [14]. In the numerical simulations, the ETB is represented by a sudden reduction of all transport coefficients to a uniform ion neo-classical level in a 3 cm wide region at the edge of the plasma. For simplicity, the width of the ETB is considered a fixed parameter. The effect of letting the ETB width vary has been studied in [15].

The theory-motivated peeling and combined ballooning–peeling ELM models defined by equations (6), (7)–(9) and (10) have been implemented in JETTO according to the same scheme as [8] uses for equation (2). At each time step, the plasma parameters calculated by JETTO are used to evaluate the mode amplitude $\xi$ given by equations (6), (7)–(9) or (10) and the calculated perturbation amplitude determines the level by which transport is enhanced. More specifically, Gaussian-shaped perturbations having amplitudes proportional to the calculated perturbation amplitude $\xi$ are added on top of the radial profiles of the transport coefficients within the ETB and its vicinity. The additional transport perturbations $\delta\chi$ representing ELMs can thus be written

$$\delta\chi(r, t) \sim \xi(t) \exp\left[-\left(\frac{r - r_0}{\Delta}\right)^2\right], \tag{11}$$

where $r_0$ is the radial location of the centre of the Gaussian and $\Delta$ is the characteristic width of the Gaussian. The use of Gaussian-shaped ELMs is motivated by the fact that the ballooning modes assumed to drive the ELMs have Gaussian shapes in linear theory.

The fact that the perturbations applied to the transport coefficients scale linearly with the calculated ballooning mode amplitude is consistent with the commonly used quasi-linear approximation [16]. In the mixing length approximation [16], which corresponds to a strong turbulence limit, the thermal conductivities and particle diffusivity scale as $\chi \sim \lambda_w^2 \gamma_d \sim \gamma_d / k_\perp^2$. Here, $\lambda_w$ is the characteristic wavelength of the turbulence, $\gamma_d$ is the decorrelation rate, which scales in the same way as the growth rate of the instability and $k_\perp$ is the perpendicular wavenumber. Therefore, the enhancement of the transport coefficients should arguably scale with the mode amplitude as something in the range from almost no dependence, consistent with the constant saturated level of diffusivity in the strong turbulence limit, to the square dependence given by the quasi-linear approximation. The linear dependence used in this paper lies in between these two extremes and gives qualitatively the same results as the quadratic dependence. As will be discussed below, the ELM amplitudes in the simulations have been limited to pre-defined peak levels, which can be thought of as a way to represent a transition to a saturated level of transport.

It turns out that it is difficult to obtain discrete peeling or combined ballooning–peeling ELMs at reasonably high edge temperatures, because slow current redistribution keeps the edge current unstable for a long time. At lower temperatures, the current can be dissipated more quickly at the edge, because the resistivity $\rho_r$ scales with the temperature $T$ as $\rho_r \sim T^{-3/2}$, whereby it becomes easier to obtain discrete ELMs. One way to make it easier to simulate peeling and combined ballooning–peeling ELMs at reasonably high edge temperatures is to

enhance the neo-classical resistivity during the ELMs. Such a scheme can be justified as a way to model the dynamo $\beta$ effect [17]. In a few simulations with high edge temperatures discussed later in this paper, neo-classical resistivity has, therefore, been enhanced during the ELMs in a similar way as the transport coefficients:

$$\delta\rho_{\mathrm{r}}(r, t) \sim \xi(t) \exp\left[-\left(\frac{r - r_0}{\Delta}\right)^2\right]. \tag{12}$$

The relative enhancement of the neo-classical resistivity is, however, usually orders of magnitude smaller than the relative enhancement of the transport coefficients. However, since the enhancement of the transport coefficients is often very large, the resistivity enhancement can also be quite significant. For instance, the ion and electron thermal conductivity and particle diffusivity are typically enhanced from an inter-ELM level of $0.2\,\mathrm{m}^2\,\mathrm{s}^{-1}$ in the ETB to a peak level of $5000\,\mathrm{m}^2\,\mathrm{s}^{-1}$ during the ELMs. The unperturbed profile of neo-classical resistivity peaks strongly at the separatrix. More specifically, the neo-classical resistivity usually varies from about $5 \times 10^{-18}\,\Omega\,\mathrm{m}$ near the top of the ETB to $6 \times 10^{-17}\,\Omega\,\mathrm{m}$ at the separatrix in the simulations described in this paper. Given the large ELM amplitude, this profile is typically perturbed during the ELMs with a Gaussian-shaped enhancement with a maximum amplitude of $5 \times 10^{-15}\,\Omega\,\mathrm{m}$. However, discrete ELMs of reasonable duration at normal edge temperatures can readily be obtained even with significantly smaller resistivity enhancements. The larger level of enhancement in this study has been used in order to shorten the ELMs and increase their frequency.

Due to a mode structure of toroidally coupled individual harmonics, ballooning and peeling modes have a global nature, even though they are controlled by localized stability criteria. In order to account for the global nature of the modes, the right-hand sides of equations (6)–(8) and (10) are treated as averages over the whole ETB in the JETTO implementation. The peeling model used in the transport simulations can thus be written

$$\frac{\mathrm{d}\xi}{\mathrm{d}t} = \frac{1}{N} \sum_{i=i_{\mathrm{top\ of\ ETB}}}^{i_{\mathrm{separatrix}}} \left[C_{\mathrm{p}}\gamma_{\mathrm{p},i}\left(1 - \frac{J_{\mathrm{c},i}}{J_i}\right)H(J_i - J_{\mathrm{c},i})\xi - C_{\mathrm{d}}\frac{c_{\mathrm{s},i}}{R_i}(\xi - \xi_0)\right] \tag{13}$$

and the combined ballooning–peeling models

$$\frac{\mathrm{d}\xi_{\mathrm{b}}}{\mathrm{d}t} = \frac{1}{N} \sum_{i=i_{\mathrm{top\ of\ ETB}}}^{i_{\mathrm{separatrix}}} \left[C_{\mathrm{b}}\gamma_{\mathrm{b},i}\left(1 - \frac{\alpha_{\mathrm{c}}}{\alpha_i}\right)H(\alpha_i - \alpha_{\mathrm{c}})\xi_{\mathrm{b}} - C_{\mathrm{d}}\frac{c_{\mathrm{s},i}}{R_i}(\xi_{\mathrm{b}} - \xi_0)\right], \tag{14}$$

$$\frac{\mathrm{d}\xi_{\mathrm{p}}}{\mathrm{d}t} = \frac{1}{N} \sum_{i=i_{\mathrm{top\ of\ ETB}}}^{i_{\mathrm{separatrix}}} \left[C_{\mathrm{p}}\gamma_{\mathrm{p},i}\left(1 - \frac{J_{\mathrm{c},i}}{J_i}\right)H(J_i - J_{\mathrm{c},i})\xi_{\mathrm{p}} - C_{\mathrm{d}}\frac{c_{\mathrm{s},i}}{R_i}(\xi_{\mathrm{p}} - \xi_0)\right], \tag{15}$$

$$\xi = \xi_{\mathrm{b}} + \xi_{\mathrm{p}} \tag{16}$$

and

$$\frac{\mathrm{d}\xi}{\mathrm{d}t} = \frac{1}{N} \sum_{i=i_{\mathrm{top\ of\ ETB}}}^{i_{\mathrm{separatrix}}} \left[C_{\mathrm{b}}\gamma_{\mathrm{b},i}\left(1 - \frac{\alpha_{\mathrm{c}}}{\alpha_i}\right)H(\alpha_i - \alpha_{\mathrm{c}})\xi + C_{\mathrm{p}}\gamma_{\mathrm{p},i}\left(1 - \frac{J_{\mathrm{c},i}}{J_i}\right)H(J_i - J_{\mathrm{c},i})\xi \right.$$
$$\left. -C_{\mathrm{d}}\frac{c_{\mathrm{s},i}}{R_i}(\xi - \xi_0)\right]. \tag{17}$$

Here, the sums run over all mesh points within the ETB, the index $i$ refers to the mesh point number and $N$ is the number of mesh points within the ETB in the JETTO grid. The choice

that the radial extent of the unstable mode usually coincides with the ETB width has been cross-checked in numerical analysis with the MHD stability code MISHKA [18].

As briefly mentioned above, the components of the total ELM amplitude resulting from the global ballooning and peeling mode equations have generally individually been limited to $5000\,\mathrm{m^2\,s^{-1}}$ in terms of ion thermal conductivity in order to take into account non-linear effects and keep the simulations numerically stable. This is the reason why the ELM amplitude is the same for each individual ELM in most of the simulations, as will be apparent later in this paper. Due to the slow redistribution of the current, the exponentially increasing ELM amplitude would grow very large without the amplitude limit before a transport relaxation would occur, which JETTO might not be able to cope with. The levels of the pressure gradient and edge current density immediately before and after the ELMs are unaffected by the limitation of the ELM amplitude, whereby the effect on ELM frequency is negligible.

For simplicity, the critical normalized pressure gradient $\alpha_c$ is radially constant in the simulations discussed in this paper. Some description of how the most important types of ELMy H-modes are controlled by various MHD stability limits is given in [3]. The fixed value $\alpha_c = 1.5$ used in this paper has been chosen so that it fairly well corresponds to the finite $n$ ballooning stability limit relevant for type I ELMy H-mode.

## 4. Simulation results

A number of predictive JETTO transport simulations making use of the ELM modelling schemes presented in section 3 are discussed in this section. All simulations use the magnetic configuration of JET discharge 53298, a typical type I ELMy H-mode discharge. The toroidal magnetic field is $B_0 = 2.67\,\mathrm{T}$ on the magnetic axis in all the simulations, as in the original discharge, and the boundary condition for the electron density at the separatrix is $n_{\mathrm{sep}} = 1 \times 10^{19}\,\mathrm{m^{-3}}$. The effective charge is $Z_{\mathrm{eff}} = 2.0$. The boundary conditions for the electron and ion temperatures vary and are stated from case to case. The neutral beam heating power and the total current also vary in some of the simulations, but are $P = 16\,\mathrm{MW}$ and $I = 2.5\,\mathrm{MA}$, respectively, unless otherwise stated. In all simulations, the ion and electron thermal conductivities and particle diffusivity are enhanced during the ELMs with Gaussian-shaped perturbations having a characteristic width of $\Delta = 6\,\mathrm{cm}$ (approximately $\Delta\rho = 0.11$ expressed in terms of the toroidal flux coordinate) and being centred at the magnetic surface $\rho = 0.92$ slightly inside the top of the ETB. The parameters of the ELM perturbation have been chosen in such a way that a very strong ballooning ELM phase can be obtained in accordance with the mechanism described in [8]. The same enhancement profiles with comparatively modest amplitudes are used for the neo-classical resistivity in the cases with resistivity enhancement applied during the ELMs. The normalized critical pressure gradient is $\alpha_c = 1.5$ and the vacuum energy parameter in the peeling stability criterion $\Delta_v = 0.2$. All simulations have been run for 0.5 s in L-mode before the transition to H-mode.

### 4.1. Reproducing type I ELMy H-mode dynamics

The theory-motivated ELM model with separate equations for the ballooning and peeling mode amplitudes given by equations (7)–(9) is capable of qualitatively reproducing the main features of type I ELMy H-mode when coupled to a JETTO transport simulation, as described in section 3. With a choice of simulation parameters consistent with actual experimental parameters, simulations with the model produce strong periodic oscillations distinctly resembling type I ELMs with a repetition frequency that increases with the external heating power. This is illustrated in frames $(a)$–$(c)$ in figure 1, which shows time traces of
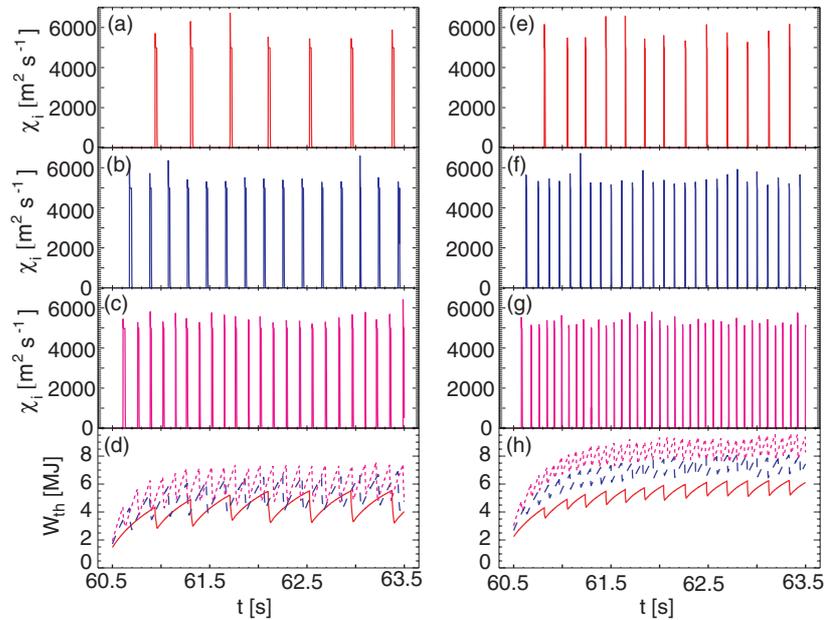
**Figure 1.** Simulations with the combined ballooning–peeling ELM model with separate equations for the ballooning and peeling mode amplitudes (equations (14)–(16)). Frames (*a*)–(*c*): ion thermal conductivity as a function of time in three mutually similar simulations with different levels of neutral beam heating power, (*a*) $P = 8$ MW, (*b*) $P = 16$ MW and (*c*) $P = 24$ MW. The boundary condition $T_{sep} = 25$ eV is used for the ion and electron temperatures at the separatrix. Neo-classical resistivity is not enhanced during the ELMs. Frame (*d*): the thermal energy content of the plasma as a function of time in the simulations used in frames (*a*) (——), (*b*) (- - - -) and (*c*) (······). Frames (*e*)–(*g*): ion thermal conductivity as a function of time in another series of simulations with different levels of neutral beam heating power, (*e*) $P = 8$ MW, (*f*) $P = 16$ MW and (*g*) $P = 24$ MW. The boundary condition $T_{sep} = 100$ eV is used for the ion and electron temperatures at the separatrix and neo-classical resistivity is enhanced during the ELMs. Otherwise, the simulation parameters are the same as in the simulations used in frames (*a*)–(*c*). Frame (*h*): the thermal energy content of the plasma as a function of time in the simulations used in frames (*e*) (——), (*f*) (- - - -) and (*g*) (······).

the ion thermal conductivity at the magnetic surface $\rho = 0.92$ in three predictive transport simulations with different levels of neutral beam heating power, namely 8, 16 and 24 MW. The plots are qualitatively similar to time traces of the $D_\alpha$ signal in type I ELMy H-mode discharges. As in experiments with type I ELMy H-mode, the ELM frequency slowly increases with the heating power. In these particular simulations, neo-classical resistivity is not enhanced during the ELMs. The boundary condition $T_{sep} = 25$ eV is used for the ion and electron temperatures at the separatrix. The feature that the level of enhancement is around 7000 m$^2$ s$^{-1}$ in terms of ion thermal conductivity is due to the limits imposed on the ELM amplitude in the ballooning and peeling mode equations.

Quantitatively, the ELMs in frames (*a*)–(*c*) in figure 1 are rather strong, as revealed in frame (*d*), which shows the thermal energy content of the plasma as a function of time in each of the three cases. Compared with experiments, the ELM frequency is rather low and each individual ELM removes a rather large fraction of the plasma energy. This is due to the very slow redistribution of the edge current, which makes the duration of the peeling unstable phase of the ELM considerably long. By enhancing neo-classical resistivity during the ELMs, the ELM frequency can be increased and the energy loss per ELM decreased to a level consistent
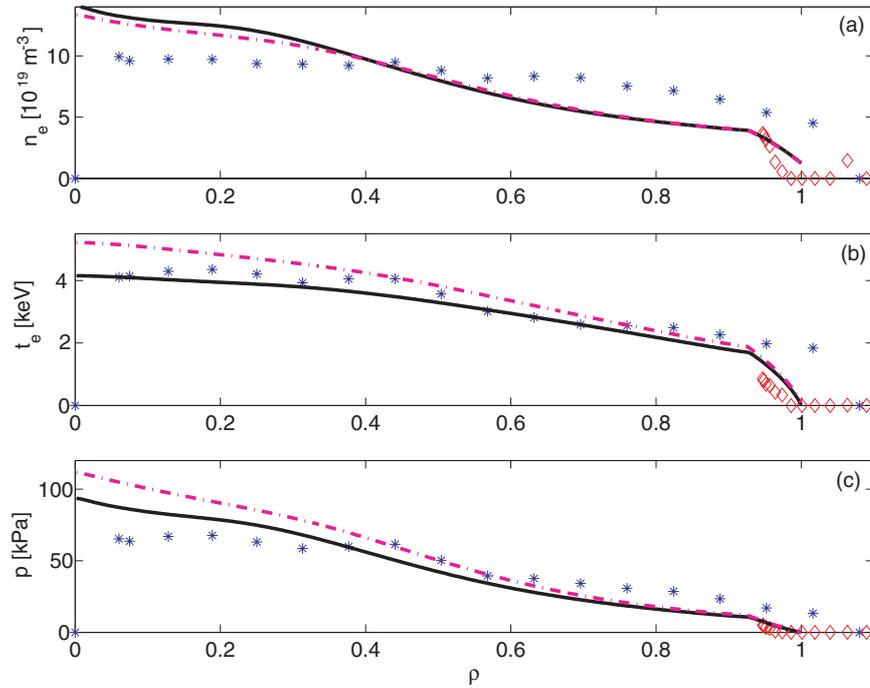
**Figure 2.** (*a*) Electron density, (*b*) electron temperature and (*c*) electron pressure profiles in two of the simulations used in figure 1 as well as experimental edge and core Lidar data from JET discharge 53298. The external heating power is roughly the same, $P = 16\,\mathrm{MW}$, in the chosen simulations as in the experimental discharge. The solid curve corresponds to the simulation in frame (*b*) in figure 1 and the dash-dotted curve to the simulation in frame (*f*) in figure 1. The diamonds indicate edge Lidar and the asterisks core Lidar data.

with experiments, even if higher edge temperature is used. This is illustrated in frames (*e*)–(*h*) in figure 1, which show a similar power scan with higher edge temperature and enhanced resistivity during the ELMs. Specifically, the edge temperature is $T_{\mathrm{sep}} = 100\,\mathrm{eV}$ for both electrons and ions and resistivity during the ELMs is enhanced from an inter-ELM peak value of $6 \times 10^{-17}\,\Omega\,\mathrm{m}$ near the separatrix to a maximum level of $5 \times 10^{-15}\,\Omega\,\mathrm{m}$.

The simulations produce reasonable pre-ELM plasma profiles in the pedestal region, despite the fact that the ELMs are rather strong, e.g. in cases without resistivity enhancement during the ELMs. Figure 2 shows the electron density, electron temperature and electron pressure profiles from the simulations used in frames (*b*) and (*f*) in figure 1 together with experimental data from JET discharge 53298, which has been used as a template in the modelling. It should be mentioned that the external heating power is roughly the same, $P = 16\,\mathrm{MW}$ in the two chosen simulations as in the experimental discharge. The plasma profiles from the simulations correspond to times shortly before an ELM, when the pressure gradient has evolved fully. The experimental data, which consist of edge and core Lidar (Thompson scattering) data, have been selected to correspond to a pre-ELM state as well as the existing data sampled at a low frequency permits. It should be noted that the data for the edge region are associated with a rather large uncertainty. In particular, the edge Lidar data probably have a rather large artificial radial shift due to the difficulty of determining location of the separatrix. Taking into account these factors and the fact that the simulations have not explicitly been intended to reproduce the plasma profiles in any particular pulse, the match with the chosen JET discharge is acceptable and shows that the calculated profiles are reasonable, as

far as the pedestal region is concerned. The large mismatch of the core profiles can be attributed
to the Bohm/gyro-Bohm transport model used in JETTO. However, it is not of primary interest
to predict the core profiles correctly in this paper, which focuses on ELM models.

### 4.2. ELM generation mechanism

When using the combined ballooning–peeling model for ELMs given by equations (14)–(16)
in JETTO, each individual ELM is normally triggered by a ballooning mode instability, which
subsequently makes the plasma peeling unstable. The ELM set off by a violation of the critical
pressure gradient continues driven by a violation of the peeling stability criterion defined by
equation (5) for a while after the pressure gradient has relaxed back to a stable level. The
ELMs in figure 1 are examples of such combined ballooning–peeling ELMs. It should be
noted that [7] reports that a single ballooning-driven ELM can trigger a cluster of peeling-
driven ELMs in simulations with an ad hoc ELM model with both ballooning and peeling
stability criteria. With the more advanced model used in this study, the result is more realistic,
namely a single strong ELM triggered by a ballooning mode instability and continuing in a
lengthy peeling phase rather than as a cluster of separate peeling mode ELMs.

Figure 3, which shows the time evolution of some plasma parameters during a typical
combined ballooning–peeling ELM, gives some insight into the dynamics of such an ELM. The
plots in the figure are derived from a simulation with the boundary condition $T_{\mathrm{sep}} = 10\,\mathrm{eV}$ for
the ion and electron temperatures at the separatrix. No resistivity enhancement is applied during
the ELMs. Specifically, frame (*a*) shows the ion thermal conductivity at the magnetic surface
$\rho = 0.92$ of maximum ELM amplitude, frame (*b*) the global ballooning mode growth rate

$$\bar{\gamma}_{\mathrm{B}} = \frac{1}{N} \sum_{i=i_{\mathrm{top\ of\ ETB}}}^{i_{\mathrm{separatrix}}} C_{\mathrm{b}} \gamma_{\mathrm{p},i} \left(1 - \frac{\alpha_{\mathrm{c}}}{\alpha_i}\right) H(\alpha_i - \alpha_{\mathrm{c}}) \tag{18}$$

and frame (*c*) the global peeling mode growth rate

$$\bar{\gamma}_{\mathrm{P}} = \frac{1}{N} \sum_{i=i_{\mathrm{top\ of\ ETB}}}^{i_{\mathrm{separatrix}}} C_{\mathrm{p}} \gamma_{\mathrm{b},i} \left(1 - \frac{J_{\mathrm{c},i}}{J_i}\right) H(J_i - J_{\mathrm{c},i}). \tag{19}$$

Frames (*d*)–(*h*) show time traces of a number of plasma parameters at three different magnetic
surfaces, namely $\rho = 0.94$, $\rho = 0.97$, and $\rho = 0.99$. To be specific, frame (*d*) shows
time traces of the normalized pressure gradient $\alpha$, frame (*e*) of the total current parallel to
the magnetic field $j_{\parallel}$, frame (*f*) of the expression $J_{\mathrm{c}}$ in the peeling mode stability criterion
defined by equation (5), frame (*g*) of the expression $J$ in the peeling mode stability criterion
and frame (*h*) of the expression $J - J_{\mathrm{c}}$.

By comparing the time traces of the ion thermal conductivity, the global ballooning mode
growth rate and the global peeling mode growth rate, it becomes clear that the ELM starts as
a ballooning mode instability and continues as a peeling mode instability. It should, however,
be noted that the critical pressure gradient is exceeded and the global ballooning mode growth
rate becomes finite already long before the discrete peak in the growth rate develops. The
complete ballooning phase is thus lengthy. Not surprisingly, the triggering of the ballooning
mode ELM phase that initiates the combined ballooning–peeling ELM follows exactly the
same mechanism as in simulations with the pure ballooning model defined by equation (2).
This mechanism is described in detail in [8]. Very briefly, the onset of a discrete ballooning
ELM phase is related to how transport is perturbed radially during the ELMs and to how the
edge pressure gradient evolves as a result of this. In order to obtain a discrete ballooning
ELM phase, the Gaussian-shaped transport perturbation applied during the ELM has to be
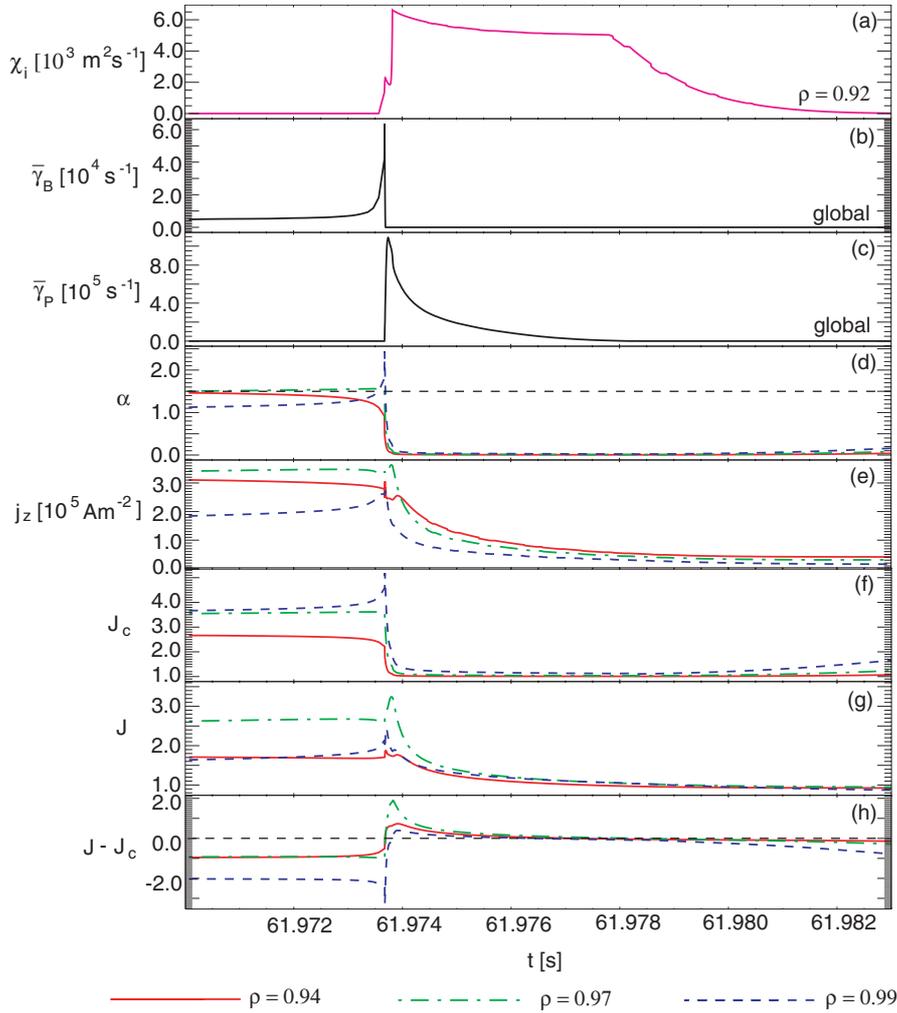
**Figure 3.** Time traces of a number of parameters of interest in a simulation with the combined ballooning–peeling ELM model with separate equations for the ballooning and peeling mode amplitudes (equations (14)–(16)): (*a*) ion thermal conductivity $\chi_i$, (*b*) global ballooning mode growth rate $\bar{\gamma}_B$, (*c*) global peeling mode growth rate $\bar{\gamma}_P$, (*d*) normalized pressure gradient $\alpha$, (*e*) toroidal current density $j_\parallel$, (*f*) the threshold $J_c$ in the peeling mode stability criterion defined by equations (3)–(5), (*g*) the expression $J$ in the peeling stability criterion, (*h*) the expression $J - J_c$. The ion thermal conductivity in frame (*a*) has been plotted at the radial location of maximum ELM amplitude, $\rho = 0.92$, whereas the quantities in frames (*c*)–(*h*) have been plotted at the magnetic surfaces $\rho = 0.94$ (——), $\rho = 0.97$ (— · —) and $\rho = 0.99$ (- - - -). In the simulation, the boundary condition $T_{sep} = 10\,eV$ is used for the ion and electron temperatures at the separatrix. Neo-classical resistivity is not enhanced during the ELMs.

centred some way inside the separatrix, e.g. at $\rho = 0.92$ as in many of the simulations in this paper, so that transport during the ELM decreases strongly towards the separatrix, whereby a strong peak in the pressure gradient builds up near the separatrix as a result of reduced heat propagation. Such a peak in the pressure gradient, clearly visible in frame (*d*) in figure 3, seems to be necessary for a discrete ELM to develop. The ballooning phase of the ELM ends only when the ELM has grown strong enough to deplete the very steep edge pressure gradient
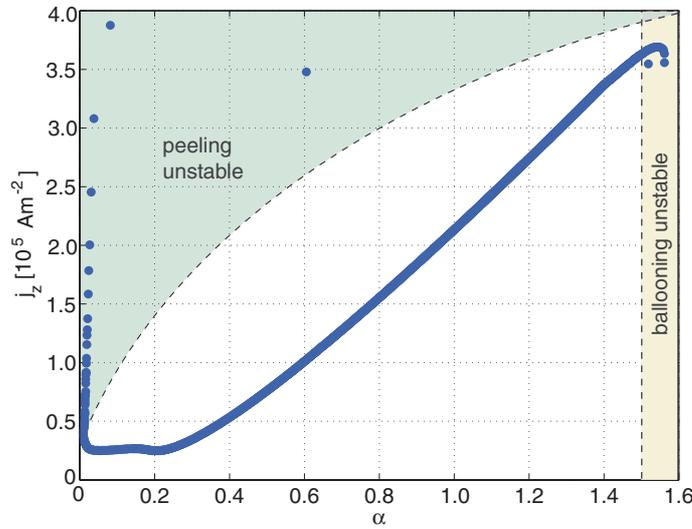
**Figure 4.** The path traced in the $\alpha$–$j_z$ operational space at the magnetic surface $\rho = 0.97$ during one ELM cycle in the simulation used in figure 3 with the combined ballooning–peeling ELM model with separate equations for the ballooning and peeling mode amplitudes (equations (14)–(16)). Consecutive points in the trace are separated by 0.1 ms. The approximate locations of the ballooning and peeling unstable domains have been indicated.

to a stable level, which happens well after the pressure gradient in the inner part of the ETB has started to relax, as frame (*d*) in figure 3 shows.

As shown in frame (*d*) in figure 3, the ballooning component of the ELM eventually becomes so strong that it starts to deplete the pressure gradient at the edge, whereby $\alpha$ falls quickly below the critical level and the ballooning mode fades away. The edge current, however, reacts more slowly to the onset of the ELM, as shown in frame (*e*) in figure 3. This is a direct consequence of the general property that the current evolves more slowly than the pressure gradient. Since the Mercier coefficient scales as $D_M \sim p'$ and generally $D_M < 0$, the stability threshold $J_c$ given by equation (4) decreases in phase with $\alpha$, as illustrated in frame (*f*) in figure 3. Because the current responds to the transport enhancement induced by the ballooning phase of the ELM more slowly than the pressure gradient, the quantity $J$ given by equation (3) remains essentially unchanged during the initial drop in $J_c$. Hence, the peeling stability criterion defined by equation (5) is violated during the collapse of $\alpha$ induced by the ballooning phase of the ELM. This becomes very evident by looking at the time trace of $J - J_c$ in frame (*h*) in figure 3. The expression $J - J_c$ exceeds zero when the initial drop in the pressure gradient occurs. At the onset of the ELM, the plasma is still deeply peeling stable.

Because of the slow redistribution of the current, it takes a relatively long time for the ELM to reduce $J$ given by equation (3) to a level below the stability threshold $J_c$. Therefore, the peeling phase of the discrete ELM peak lasts noticeably longer than the brief large-amplitude phase of ballooning instability preceding it. The feature that the decay time of the ELM is of the order of or longer than both the peak ballooning phase and the peeling phase of the ELM is due to the fact that the damping rate term in equation (10) is much smaller than the ballooning and peeling mode growth rate terms, as determined by the choices $C_d \ll C_b$ and $C_d \ll C_p$.

Each ELM cycle follows a characteristic path in the operational space defined by the normalized pressure gradient and the edge current density, as illustrated in figure 4. The figure shows a trace made up of points ($\alpha$, $j_z$) at the magnetic surface $\rho = 0.97$ sampled over

one ELM cycle lasting 120 ms in the simulation used in figure 3. Here, $j_z$ is the toroidal current density. Consecutive points in the trace have an equidistant temporal separation of $1 \times 10^{-4}$ s. The ballooning unstable region bounded by a vertical line at $\alpha = 1.5$ and the approximate location of the peeling unstable region are indicated in the plot. As expected, figure 4 confirms the qualitative results observed when discussing figure 3. The ELM cycle starts with the lengthy build-up of the pressure gradient and the edge current density. Because the pressure gradient generally evolves faster than the current and because peeling modes are stabilized by an increase in the pressure gradient, the first stability criterion to be violated is the ballooning stability limit defined by the critical pressure gradient. Even after the ballooning stability limit has been exceeded, the pressure gradient continues to increase for some time, which corresponds to the situation in which an ever stronger peak in the pressure gradient builds up at the edge due to the reduction of transport towards the separatrix caused by the shape and localization of the ELM perturbation. The collapse of the pressure gradient is extremely fast, lasting less than 0.2 ms once it starts, as indicated by the large distance between the points in the plot during this phase. The diagram unambiguously shows that it is the drop in the pressure gradient that makes the plasma peeling unstable. The collapse of the edge current takes a considerably longer time than the collapse of the pressure gradient and starts only when the pressure gradient has relaxed almost fully. It should be noted that the ELM cycle obtained here resembles the cycle for type I ELMs predicted in [20].

### 4.3. Pure ballooning and pure peeling mode ELMs

For a large range of parameters, the combined ballooning–peeling model given by equations (14)–(16) generates ELMs with a ballooning mode phase followed by a peeling mode phase. However, in some situations such as with a low or a high level of current, the model can generate either pure ballooning or pure peeling mode ELMs, respectively. This is illustrated in figure 5, which demonstrates typical ELM behaviour in situations with current ramp-up and ramp-down. Frame (*a*) shows the total plasma current as a function of time in a simulation with an initial 1.5 s long phase with a constant current of $I = 2.5$ MA followed by a current ramp-up at a rate of $dI/dt = 1.0$ MA s$^{-1}$ to $I = 4.0$ MA, frame (*b*) the ion thermal conductivity at the magnetic surface $\rho = 0.92$, frame (*c*) the global ballooning mode growth rate $\bar{\gamma}_B$, frame (*d*) the global peeling mode growth rate $\bar{\gamma}_P$ and frame (*e*) the thermal energy content. Frames (*f*)–(*j*) show the same quantities in a simulation with an initial 1.5 s long phase with a constant current of $I = 3.0$ MA followed by a current ramp-down at a rate of $dI/dt = -1.0$ MA s$^{-1}$ to $I = 1.5$ MA. In both simulations, the boundary condition $T_{sep} = 10$ eV is used for both ion and electron temperatures at the separatrix. Neo-classical resistivity is not enhanced during the ELMs.

The time traces of the global ballooning and peeling mode growth rates indicate that during the initial phases of constant current each ELM is triggered by a ballooning mode instability and continues in a peeling unstable phase in both simulations. In the simulation with current ramp-up, the ELMs, with a few exceptions, change into pure peeling mode ELMs after the start of the ramp-up. There are two reasons for the immediate transition to pure peeling mode ELMs. First, the edge current responds very quickly to the ramp-up, bringing the plasma towards the peeling instability threshold. Second, the poloidal magnetic field increases with increasing current. Since $\alpha$ decreases with increasing poloidal magnetic field, the current ramp-up effectively reduces the level of $\alpha$, so that a higher level of (unnormalized) pressure gradient is needed to reach $\alpha_c$. The ELM frequency during the ramp-up is lower than during the phase of steady current due to the effect of the poloidal magnetic field on $\alpha$, which prevents ballooning stability from being violated at an early stage. The thermal energy content increases
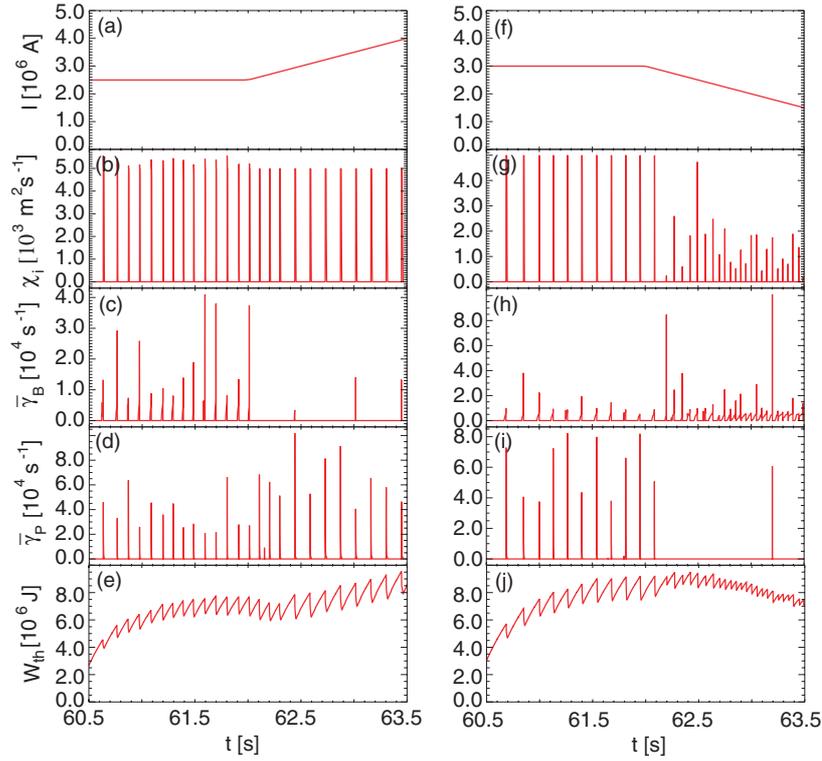
**Figure 5.** Current ramp-up and ramp-down in simulations with the combined ballooning–
peeling ELM model with separate equations for the ballooning and peeling mode amplitudes
(equations (14)–(16)). The left-hand column corresponds to a simulation with an initial 1.5 s
long phase with a constant current of $I = 2.5$ MA followed by a current ramp-up at a rate of
$dI/dt = 1.0$ MA s$^{-1}$ to $I = 4.0$ MA and the right-hand column to a simulation with an initial 1.5 s
long phase with a constant current of $I = 3.0$ MA followed by a current ramp-down at a rate of
$dI/dt = -1.0$ MA s$^{-1}$ to $I = 1.5$ MA. The following time traces are shown: frames (a) and (f):
total plasma current $I$. Frames (b) and (g): ion thermal conductivity $\chi_i$ at the magnetic surface
$\rho = 0.92$. Frames (c) and (h): global ballooning mode growth rate $\bar{\gamma}_B$. Frames (d) and (i): global
peeling mode growth rate $\bar{\gamma}_P$. Frames (e) and (j): thermal energy content $W_{th}$. In both simulations,
the boundary condition $T_{sep} = 10$ eV is used for the ion and electron temperatures at the separatrix.
Neo-classical resistivity is not enhanced during the ELMs.

during the current ramp-up, because the (unnormalized) pedestal pressure gradient, contrary
to $\alpha$, evolves to larger values than during the steady current phase due to the lower ELM
frequency. As a result of profile stiffness, the steeper pedestal pressure gradient translates into
a larger total energy content. It should be noted that with higher levels of initial current, pure
peeling mode ELMs are obtained already during the phase with steady current, whereby a
ramp-up causes the ELM frequency to increase.

In the simulation with current ramp-down, the ELMs, with a few exceptions, change into
pure ballooning mode ELMs after the start of the ramp-down. The main reason for the transition
to pure ballooning mode ELMs is that the current ramp-down quickly reduces the edge current
to such a low level that the collapse of the pressure gradient due to a ballooning mode ELM is
not enough to make the plasma peeling unstable. In addition, the ELMs tend to occur for lower
levels of edge pressure gradient and edge current density during the ramp-down because of an
increase in the level of $\alpha$ due to the decreasing poloidal magnetic field. This together with the

features that the pure ballooning mode ELMs are both shorter and have smaller amplitudes than the combined ballooning–peeling mode ELMs causes the ELM frequency to increase significantly at the transition to pure ballooning mode ELMs. The thermal energy content decreases during the current ramp-down, because the ELMs are triggered for lower values of the pedestal pressure gradient than during the steady current phase due to both the increased ELM frequency and the reduced poloidal magnetic field.

It should be noted that pure ballooning and peeling mode ELMs can be observed in other situations as well. Apart from the edge current density, parameters such as the normalized critical pressure gradient $\alpha_c$, the vacuum energy parameter $\Delta_v$ and the normalization of the growth rates determined by the constants $C_b$ and $C_p$ influence whether combined ballooning–peeling or pure ballooning or peeling mode ELMs are obtained.

### 4.4. Sensitivity with respect to ballooning and peeling mode growth rates

An interesting feature of the combined ballooning–peeling model given by equations (14)–(16) is that the simulation results obtained with it are both qualitatively and quantitatively relatively insensitive to the ballooning and peeling mode growth rates. The sensitivity to the growth rates has been studied by fixing the characteristic growth rate coefficients at $\gamma_p = \gamma_b = c_s/\sqrt{L_p R}$ and systematically varying the arbitrary constants $C_b$ and $C_p$ in the growth rate terms in equations (14) and (15), respectively. The results of these parameter scans are illustrated in figure 6, which shows time traces of the ion thermal conductivity at the magnetic surface $\rho = 0.92$ of maximum ELM amplitude in a number of simulations with the combined ballooning–peeling model. In the left-hand column of the figure, $C_p = 1.0$ and $C_b$ varies as follows: (a) $C_b = 1.0 \times 10^{-2}$, (b) $C_b = 1.0 \times 10^{-1}$, (c) $C_b = 1.0$, (d) $C_b = 1.0 \times 10^2$, (e) $C_b = 1.0 \times 10^4$. In the right-hand column, $C_b = 1.0$ and $C_p$ varies as follows: (f) $C_p = 1.0 \times 10^{-2}$, (g) $C_p = 1.0 \times 10^{-1}$, (h) $C_p = 1.0$, (i) $C_p = 1.0 \times 10^2$, (j) $C_p = 1.0 \times 10^4$. Otherwise, the simulation parameters are the same in all ten simulations. In particular, the boundary condition $T_{sep} = 25\,\text{eV}$ is used for the ion and electron temperatures at the separatrix. Neo-classical resistivity is not enhanced during the ELMs.

The ELM frequency initially increases with increasing ballooning mode growth rate, but then stabilizes for $C_b \gtrsim 1 \times 10^{-1}$. With respect to the peeling mode growth rate the ELM frequency is equally insensitive in a similar parameter range, $C_b \gtrsim 1 \times 10^{-1}$. For $C_b \lesssim 1 \times 10^{-2}$, the combined ballooning–peeling model generates almost pure ballooning mode ELMs, whereby the ELM amplitude drops and the ELM frequency increases dramatically, as visible in frame (j) in figure 6. It should be emphasized that the parameter ranges for $C_b$ and $C_p$ used in figure 6 are very large. Within, for instance, the parameter space $0.1 \leqslant C_b \leqslant 10$, $0.1 \leqslant C_p \leqslant 10$, which is of most interest, the ELM frequency is practically constant. It turns out that the pre-ELM level of the thermal energy content is also remarkably constant in the simulations belonging to this parameter range. Only in the simulations used in frames (a) and (f) are noticeably higher levels of thermal energy content achieved. In the former case, the ELMs have so weak a ballooning component that they do not manage to deplete the pressure gradient to a stable level, whereby higher pedestal pressure and thus better performance are obtained. In the latter case, the peeling component of the ELMs is very weak, which leads to quite small and benign ELMs. As a result of this, the pedestal recovers more fully from the ELMs. In other words, a steep pressure gradient is obtained throughout the pedestal before an ELM is triggered, which explains why the plasma performance is slightly better than in the cases with very strong combined ballooning–peeling ELMs. In conclusion, it is justified to use the same characteristic growth rate for ballooning and peeling modes in the ELM models presented in section 2.
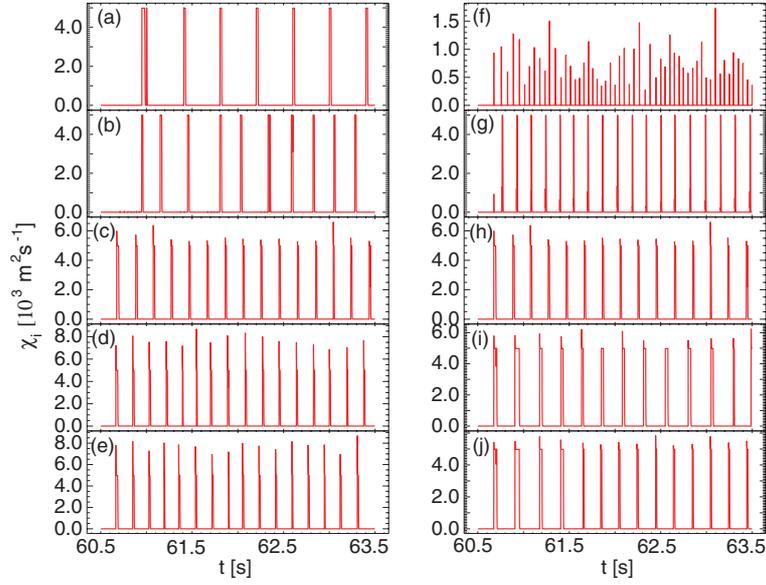
**Figure 6.** Time traces of ion thermal conductivity at the magnetic surface $\rho = 0.92$ of maximum ELM amplitude in simulations with the combined ballooning–peeling ELM model with separate equations for the ballooning and peeling mode amplitudes (equations (14)–(16)). The scaling factors in the ballooning and peeling mode growth rate terms have been varied as follows, while the characteristic ballooning and peeling mode growth rates have been kept fixed at $\gamma_p = \gamma_b = c_s/\sqrt{L_p R}$: (a) $C_b = 1.0 \times 10^{-2}$, $C_p = 1.0$; (b) $C_b = 1.0 \times 10^{-1}$, $C_p = 1.0$; (c) $C_b = 1.0$, $C_p = 1.0$; (d) $C_b = 1.0 \times 10^2$, $C_p = 1.0$; (e) $C_b = 1.0 \times 10^4$, $C_p = 1.0$; (f) $C_b = 1.0$, $C_p = 1.0 \times 10^{-2}$; (g) $C_b = 1.0$, $C_p = 1.0 \times 10^{-1}$; (h) $C_b = 1.0$, $C_p = 1.0$; (i) $C_b = 1.0$, $C_p = 1.0 \times 10^2$; (j) $C_b = 1.0$, $C_p = 1.0 \times 10^4$. Otherwise, the simulation parameters are the same in all ten simulations. In particular, the boundary condition $T_{sep} = 25$ eV is used for the ion and electron temperatures at the separatrix. Neo-classical resistivity is not enhanced during the ELMs.

## 4.5. Simulations with a one-equation ballooning–peeling model

It turns out that the one-equation ballooning–peeling model given by equation (17) almost always reproduces the same behaviour as the model with separate equations for ballooning and peeling modes given by equations (14)–(16). This is shown in figure 7, which illustrates the results of parameter scans with the one-equation ballooning–peeling model given by equation (17) completely analogous to those shown in figure 6. Specifically, the parameters $C_b$ and $C_p$ vary in the same way from frame to frame in figure 7 as in figure 6 and the remaining simulation parameters are exactly the same in all simulations in both figures, i.e. as given in section 4.4. Hence, the two figures can be compared directly and it is evident that both models produce qualitatively the same kind of behaviour. In particular, both models generate pure ballooning mode ELMs with $C_b = 1.0$ and $C_p = 1.0 \times 10^{-2}$. Quantitatively, the difference in ELM frequency is small in all ten comparisons of simulations with the two models. The fact that the model with separate equations for ballooning and peeling modes gives a slightly larger ELM amplitude than the one-equation ballooning–peeling model is due to the fact that the ELM amplitudes have been limited separately in each equation to 5000 m$^2$ s$^{-1}$ in terms of ion thermal conductivity in the former case and the combined ballooning–peeling ELM amplitude to the same value in the latter case. It should be emphasized that the qualitatively and quantitatively similar behaviour produced by the two models is a general result, which applies not only in the parameter scans shown in figures 6 and 7, but in most situations.
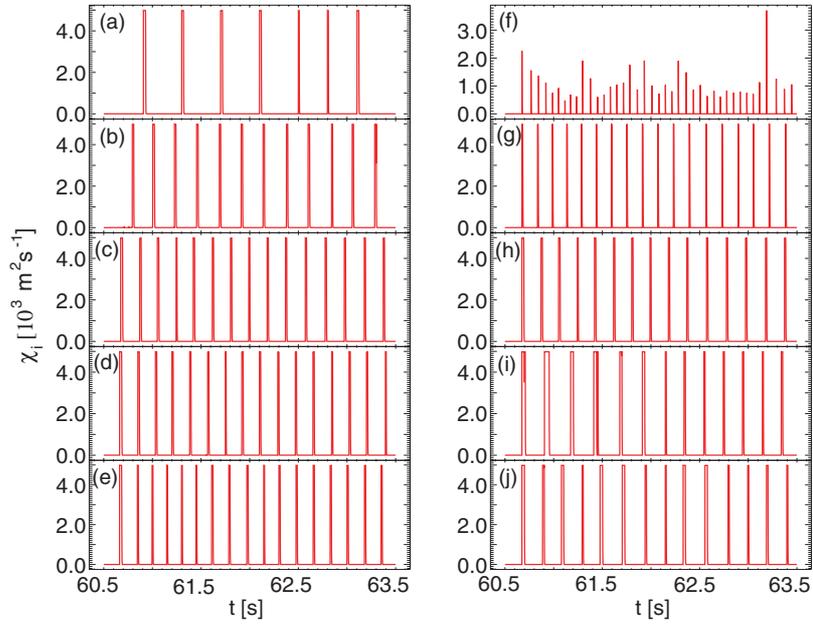
**Figure 7.** Time traces of the ion thermal conductivity at the magnetic surface $\rho = 0.92$ of maximum ELM amplitude in simulations with the combined ballooning–peeling ELM model with a single equation for a combined ballooning–peeling mode amplitude (equation (17)). The scaling factors in the ballooning and peeling mode growth rate terms have been varied exactly in the same way as in figure 6 in frames (a)–(j) and all the other simulation parameters are also exactly the same as in the simulations in figure 6.

### 4.6. Simulations with a peeling stability criterion only

The theory-motivated pure peeling model described by equation (6) can in a similar way as the combined ballooning–peeling models produce periodic discrete oscillations qualitatively resembling type I ELMs when coupled to a transport simulation as described in section 3. The frequency of these relaxations increases with increasing external heating power, as in experiments with type I ELMs. Frames (a)–(c) in figure 8 show the ELM behaviour in three simulations with different levels of neutral beam heating power. To be specific, the neutral beam heating power is $P = 8$ MW in frame (a), $P = 16$ MW in frame (b) and $P = 24$ MW in frame (c). The boundary condition $T_{sep} = 100$ eV is used for the electron and ion temperatures at the separatrix. Neo-classical resistivity is enhanced during the ELMs. Since the simulation parameters in this power scan are exactly the same as in the power scan illustrated in frames (e)–(g) in figure 1, the two series of simulations can be compared directly. Noticeably, the ELM frequency is much lower in the case of ELMs controlled solely by peeling mode stability than in the case of ELMs controlled by both ballooning and peeling modes, because in the absence of a ballooning stability criterion, the plasma continues to evolve until it reaches the peeling stability limit, whereby an ELM occurs. The pure peeling mode ELMs are longer than the combined ballooning–peeling ELMs, since they start off at a higher level of edge current than the ELMs triggered by the pressure gradient and it takes a long time for them to deplete the current to a stable level. Quantitatively, the edge current density and edge pressure gradient typically both reach values twice as high as in figure 4, but otherwise the pure peeling ELM cycle resembles the combined ballooning–peeling ELM cycle with a very fast collapse of the edge pressure gradient followed by a slower depletion of the edge current.
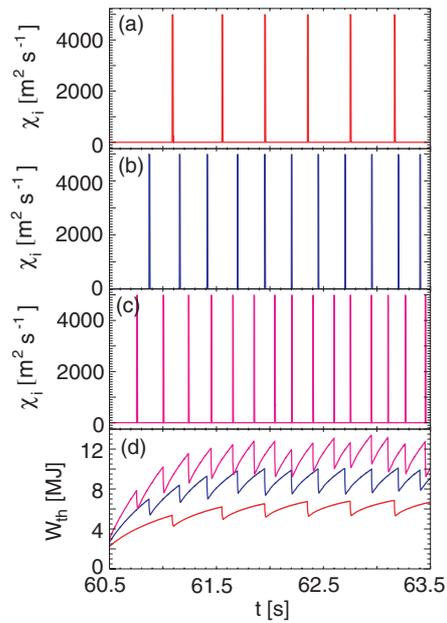
**Figure 8.** Simulations with the pure peeling mode ELM model (equation (13)). Frames (*a*)–(*c*): ion thermal conductivity as a function of time in three mutually similar simulations with different levels of neutral beam heating power, (*a*) $P = 8$ MW, (*b*) $P = 16$ MW and (*c*) $P = 24$ MW. The boundary condition $T_{sep} = 100$ eV is used for the ion and electron temperatures at the separatrix and neo-classical resistivity is enhanced during the ELMs. Frame (*d*): the thermal energy content of the plasma as a function of time in the simulations used in frames (*a*)–(*c*).

In accordance with the long ELM duration, the drop in thermal energy content resulting from each ELM is very large, as shown in frame (*d*) in figure 8. By centring the ELM perturbation not in the vicinity of the top of the ETB, as here, but closer to the separatrix, so that it more effectively increases transport in the pedestal, the ELM frequency can be increased slightly, but it is still difficult to quantitatively reproduce experimental ELM frequencies with the pure peeling model.

## 5. Summary and discussion

This paper has presented a theory-motivated model for type I ELMy H-mode based on linear ballooning and peeling mode stability theory. In the model, a total mode amplitude is calculated as a sum of the individual mode amplitudes given by two separate linear differential equations for the ballooning and peeling mode amplitudes, respectively. The ballooning and peeling mode growth rates are represented by mutually analogous terms in the individual equations. A critical pressure gradient and a peeling mode stability criterion, respectively, control whether the growth rate terms differ from zero. The damping of the modes due to non-ideal MHD effects is controlled by a term tending to drive the mode amplitude back towards the level of background fluctuations. The ELM model has been coupled to the JETTO transport code in such a way that the calculated total mode amplitude linearly determines the level of transport enhancement in the pedestal region. In order to account for the fact that ballooning and peeling modes are global, the differential equations defining the model are averaged over the whole ETB in the JETTO implementation.

It has been demonstrated that the ELM model qualitatively reproduces the experimental dynamics of type I ELMy H-mode, including an ELM frequency that increases with the external heating power. The pre-ELM plasma profiles are also reproduced reasonably well, despite the fact that the ELMs are rather strong in many situations. The typical ELM cycle reproduced by the model has been examined in close detail. It turns out that the individual ELMs are usually driven by both ballooning and peeling mode instabilities. Due to the fact that the current generally evolves more slowly than the pressure gradient, the combined ballooning–peeling mode ELMs are triggered by a violation of the ballooning stability criterion. The collapse of the pressure gradient induced by the ballooning phase of the ELM then leads to a violation of the peeling mode stability criterion and the ELM continues in a generally quite long peeling mode phase until the edge current density has been depleted to a stable level. It has been shown that alternative ELM cycles with pure peeling and pure ballooning ELMs can be obtained, e.g. in situations with current ramp-up and ramp-down, respectively. It has also been demonstrated that the behaviour reproduced by the ELM model is very insensitive with respect to both the ballooning and peeling mode growth rates.

An alternative ELM model with a single linear differential equation for a combined ballooning–peeling mode amplitude has also been introduced. It has been shown that simulations with this model reproduce essentially the same behaviour as modelling with separate equations for the ballooning and peeling mode amplitudes. Similarly, a simplified model with a peeling mode stability criterion only has been explored. It turns out that this model too can qualitatively reproduce the experimental dynamics of type I ELMy H-mode. However, because of the very slow redistribution of the current, it is difficult to quantitatively reproduce, e.g. experimentally observed ELM frequencies and ELM energy losses with the pure peeling mode model.

## Acknowledgment

## References

[1] Connor J W 1998 *Plasma Phys. Control. Fusion* **40** 531
[2] Suttrop W 2000 *Plasma Phys. Control. Fusion* **42** A1
[3] Lönnroth J-S *et al* 2003 *Plasma Phys. Control. Fusion* **45** 1689
[4] Parail V *et al* 2002 *Proc. 19th IAEA Fusion Energy Conf. (Lyon, France, 14–19 October 2002)*
[5] Parail V *et al* 2003 *Plasma Phys. Rep.* **29** 539
[6] Lönnroth J-S *et al* 2004 *Plasma Phys. Control. Fusion* **46** 767
[7] Onjun T *et al* 2003 *Phys. Plasmas* submitted
[8] Lönnroth J-S *et al* 2004 *Plasma Phys. Control. Fusion* **46** A249
[9] Lebedev V B *et al* 1995 *Phys. Plasmas* **2** 3345
[10] Connor J W, Hastie R J, Wilson H R and Miller R L 1998 *Phys. Plasmas* **5** 2687
[11] Mercier C 1960 *Nucl. Fusion* **1** 47
[12] Mercier C 1962 *Nucl. Fusion* **2** (Suppl.) 801
[13] Cennachi G and Taroni A 1988 JET-IR(88) 03
[14] Erba M *et al* 1997 *Plasma Phys. Control. Fusion* **39** 261
[15] Onjun T, Bateman G, Kritz A H and Hammet G 2002 *Phys. Plasmas* **9** 5018
[16] Weiland J 2000 *Collective Modes in Inhomogeneous Plasmas* (Bristol, UK: Institute of Physics Publishing)
[17] Biskamp D 1997 *Nonlinear Magnetohydrodynamics* (Cambridge, UK: Cambridge University Press)
[18] Huysmans G T A, Sharapov S E, Mikhailovskii A B and Kerner W 2001 *Phys. Plasmas* **10** 4292
[19] Mikhailovskii A B *et al* 1997 *Plasma Phys. Rep.* **23** 844
[20] Snyder P B *et al* 2002 *Phys. Plasmas* **9** 2037